AGU PUBLICATIONS

JGR

Journal of Geophysical Research: Oceans

RESEARCH ARTICLE

10.1002/2016JC011911

Key Points:
- Red Sea is highly sensitive to dust-induced reduction in radiative fluxes
- Dust aerosols are important in regulating surface and subsurface temperature of the Red Sea
- Quantitative estimate of dust-induced thermal cooling of Red Sea

Correspondence to:
B. Cahill,
bronwyn.cahill@io-warnemuende.de

Citation:
Cahill, B., R. Toumi, G. Stenchikov, S. Osipov, and H. Brindley (2017), Evaluation of thermal and dynamic impacts of summer dust aerosols on the Red Sea, *J. Geophys. Res. Oceans*, *122*, 1325–1346, doi:10.1002/2016JC011911.

Received 22 APR 2016
Accepted 21 DEC 2016
Accepted article online 6 JAN 2017
Published online 20 FEB 2017

Evaluation of thermal and dynamic impacts of summer dust aerosols on the Red Sea

Bronwyn Cahill[1,2], Ralf Toumi[1], Georgiy Stenchikov[3], Sergey Osipov[3], and Helen Brindley[1]

[1]Space and Atmospheric Physics, Imperial College London, London, UK, [2]Now at Leibniz Institute for Baltic Sea Research, Warnemünde, Germany, [3]Division of Physical Sciences and Engineering, King Abdullah University of Science and Technology, Thuwal, Kingdom of Saudi Arabia

Abstract The seasonal response of upper ocean processes in the Red Sea to summer-time dust aerosol perturbations is investigated using an uncoupled regional ocean model. We find that the upper limit response is highly sensitive to dust-induced reductions in radiative fluxes. Sea surface cooling of −1°C and −2°C is predicted in the northern and southern regions, respectively. This cooling is associated with a net radiation reduction of −40 W m^{-2} and −90 W m^{-2} over the northern and southern regions, respectively. Larger cooling occurs below the mixed layer at 75 m in autumn, −1.2°C (north) and −1.9°C (south). SSTs adjust more rapidly (ca. 30 days) than the subsurface temperatures (seasonal time scales), due to stronger stratification and increased mixed layer stability inhibiting the extent of vertical mixing. The basin average annual heat flux reverses sign and becomes positive, +4.2 W m^{-2} (as compared to observed estimates −17.3 W m^{-2}) indicating a small gain of heat from the atmosphere. When we consider missing feedbacks from atmospheric processes in our uncoupled experiment, we postulate that the magnitude of cooling and the time scales for adjustment will be much less, and that the annual heat flux will not reverse sign but nevertheless be reduced as a result of dust perturbations. While our study highlights the importance of considering coupled ocean-atmosphere processes on the net surface energy flux in dust perturbation studies, the results of our uncoupled dust experiment still provide an upper limit estimate of the response of the upper ocean to dust-induced radiative forcing perturbations.

1. Introduction

The Red Sea is located in the heart of the dust belt between the Arabian Peninsula and Saharan Desert, both major dust sources which account for about half of global dust emissions [*Prospero et al.*, 2002]. In the Arabian Peninsula, dust storms (short-lived) and blowing dust (persistent background dust) are frequent events throughout most of the year, but in summer, large amounts of mineral dust from the Arabian Peninsula and North Africa are transported across the Red Sea and Arabian Sea [*Li and Ramanathan*, 2002] with the onset of the southwest monsoon.

Dust aerosols play an important role in regulating the thermal and chemical balances of the oceans by directly interacting with both shortwave and longwave radiation, thus influencing the transport of energy across the atmosphere-ocean boundary, modifying the air circulation over the sea, and delivering nutrients through dust deposition [*Jaing et al.*, 2009; *Kalenderski et al.*, 2013; *Prakash et al.*, 2015]. While quantifying the impact of dust aerosols on the Earth's climate remains a challenge, their effect is potentially significant for the circulation and heat budget of regional seas over different time scales.

Lau and Kim [2007] show that there is a robust negative correlation between atmospheric dust loading and Atlantic SST consistent with the view that westward transport of Saharan dust is associated with cooling of the Atlantic during the early hurricane season. Modeling studies of wintertime dust outbreaks over the Arabian Peninsula [using the Weather Research and Forecast Model, *Skamarock et al.*, 2007] coupled with the chemistry module (WRF-Chem) [*Grell et al.*, 2005] have examined the effect of dust aerosols on shortwave and longwave radiation transport and the reduction in surface energy balance over the Red Sea [*Kalenderski et al.*, 2013]. They find a wintertime daily mean reduction in surface solar radiation of −6 W m^{-2} but an instantaneous solar radiance reduction of almost −100 W m^{-2} just under a dust aerosol plume. This is equivalent to a reduction in the surface energy balance by about a quarter of the incoming solar flux.

Prakash et al. [2015] similarly modeled a springtime dust storm over the Arabian Peninsula and Red Sea and found the maximum daily average shortwave and longwave direct radiative effects at the surface to be -134 W m^{-2} and $+43$ W m^{-2}, respectively. Daily domain averaged values of shortwave and longwave direct radiative effects at the surface were -16 W m^{-2} and $+6$ W m^{-2}, respectively.

Brindley et al. [2015] have assessed the climatological aerosol loading and associated cloud free aerosol direct radiative effect over the Red Sea using a combination of ground-based and satellite observations in conjunction with a Rapid Radiative Transfer Model (RRTM). They find the seasonal impact of dust aerosols on the shortwave direct radiative forcing averaged over the Red Sea to be significantly larger than the findings of *Kalenderski et al*. [2013] and *Prakash et al*. [2015], with daily mean values of -31.8 W m^{-2} in winter and -54.5 W m^{-2} in spring. Overall, *Brindley et al*. [2015] estimates of climatological dust direct radiative effect exhibit enhanced aerosol loading and the development of a north to south gradient in the summer relative to the winter months over the region. Shortwave cooling typically dominates the net radiative effect over the basin and is particularly pronounced in summer in the southern Red Sea, reaching -120 W m^{-2} at the surface (Figure 2). A similar north to south gradient is seen in the coincident longwave heating in summer in the southern Red Sea, which is on the order of $+30$ W m^{-2} at the surface (Figure 2), reducing the total dust-induced radiative cooling of the sea surface in the southern Red Sea in summer to -90 W m^{-2} (Figure 2).

While the *Brindley et al*. [2015] estimates of dust aerosol induced reduction in radiative forcing are significantly larger than those found in earlier modeling investigations [*Prakash et al*., 2015; *Kalenderski et al*., 2013], it is important to note that these earlier studies report on radiative forcing over land for short-term dust events in winter and spring only. The *Brindley et al*. [2015] climatology, which incorporates ground-based observations and 5 years of satellite retrievals, provides a comprehensive seasonal view of cloud-free dust radiative effects over the sea, where aerosol surface cooling will be larger than over the desert due to the very small albedo of the ocean compared to that of the desert [*Osipov et al*., 2015]. Moreover, the *Brindley et al*. [2015] findings highlight the importance of summer as the period of maximum dust loading over the sea basin and underline the stronger impact of dust loading in the southern Red Sea. This is consistent with the aerosol optical depth estimates of *Li and Ramanathan* [2002] over the northern Arabian Sea and the observation that large amounts of mineral dust from the Arabian Peninsula and North Africa are transported across the Red Sea and Arabian Sea with the onset of the southwest monsoon. *Prospero et al*. [2002] also identify summertime, May–July, as the period of maximum dust activity over the Red Sea.

Significant cooling of surface waters is expected in response to this scale of reduction in the surface energy balance in the summer indicating the profound role dust aerosols potentially play in regulating the sea surface temperature of the Red Sea. In this paper, we present an upper limit sensitivity study in which the magnitude of surface and subsurface cooling in the Red Sea in response to summer-time dust aerosol perturbations is quantified using a regional ocean model. So far, the dust impact on the Red Sea has not been accounted for in modeling studies. Here we show quantitatively the potential importance of this effect on the short-term seasonality of upper ocean processes. In section 2, we provide an overview of the study location and key circulation features and heat budget estimates. In section 3, we describe the regional ocean model, the configuration of our uncoupled dust aerosol perturbation experiments and clarify the simplifications of our sensitivity study. In section 4, we present the modeled seasonal cycle of the heat flux components and the baseline ocean state, and then assess the impact of summer-time dust aerosols on ocean state and heat budget. We elucidate the different time scales of adjustment for the surface and subsurface temperature fields, the response of the surface longwave, latent, and sensible heat fluxes to dust-induced cooling, and the changes to mesoscale circulation features and transport. Finally, we discuss the significance of our findings and their limitations. We infer a zeroth-order approximation of the energy balance for a coupled ocean-atmosphere scenario and draw some conclusions. To our best knowledge, it is the first such investigation, which captures the three-dimensional scope of the Red Sea's response to dust aerosols.

2. Study Location

The Red Sea is an elongated semi-enclosed basin centred around 21°N and 38°E, flanked by Saudi Arabia and the Yemen on its eastern side and Egypt, Sudan and Eritrea on its western side. It is approximately 2000 km long and 220 km wide. It has an average depth of 490 m with a deep trench carved into the meridional axis of the basin, where depths can exceed 2000 m (Figure 1). It is connected to the Arabian Sea and

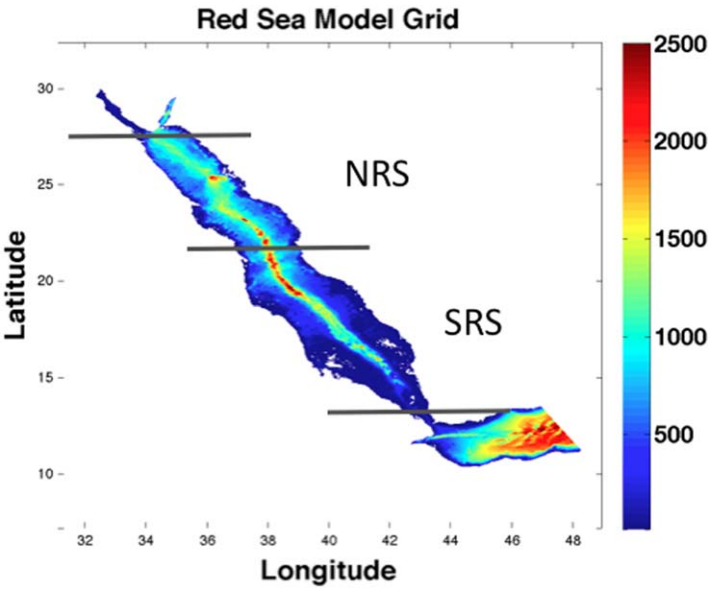

Figure 1. Red Sea model domain and delimitation of North Red Sea (NRS) and South Red Sea (SRS) subregions used in the analysis.

Indian Ocean via the Gulf of Aden through the strait of Bab el Mandeb, a very narrow (ca. 25 km) and shallow (sill depth is ca. 160 m) channel.

The Red Sea is the home to one of the most diverse marine ecosystems in the world, which has adapted a delicate balance to live in one of the most saline and warmest seas in the world [*Baars et al.*, 1998; *Belkin*, 2009; *Raitsos et al.*, 2011, 2013]. Its high surface salinity, >41 PSU in its northern basin, is caused by an intense evaporation rate, with recent estimates ranging from 1.76 ± 0.35 m yr^{-1} [*Tragou et al.*, 1999] to 2.06 ± 0.22 m yr^{-1} [*Sofianos et al.*, 2002].

Its large-scale circulation is governed by strong thermohaline and wind forcing [*Quadfasel and Baudner*, 1993]. High surface salinities coupled with winter cooling, drive a thermohaline flow in the upper and deep layers in the north [*Phillips*, 1966]. In the central and southern basin, atmospheric forcing, dominated by bi-annually reversing monsoon winds, gives rise to seasonally changing patterns in the upper layer circulation [*Patzert*, 1974]. Throughout the year, the wind direction north of 19°N is predominantly north-northwesterly. South of 19°N, the winds are controlled by the monsoon system of the Arabian Sea. During the winter northeast monsoon (October–May), the wind direction is south-southeasterly, and the surface inflow from the Gulf of Aden through the Bab el Mandeb is enhanced. A simple two-layer flow persists with a relatively fresh inflow on top of a deep hypersaline outflow originating from the northern basin. During the summer southwest monsoon (June–September), the wind direction is north-northwesterly, and there is a transition from a two-layer exchange flow to a more complex three layer exchange pattern [*Murray and Johns*, 1997]. Summer-time observations by *Sofianos and Johns* [2007] reveal a very intense and complicated circulation pattern in the Red Sea. The northern basin is characterized by a permanent, cyclonic feature, which plays an important role in the production of Red Sea Overflow Water (RSOW). This water mass is one of the most saline water masses observed in the world ocean. It results from the very high evaporation rate (in excess of 2 m yr^{-1}, *Sofianos et al.*, [2002]) in the Red Sea and is thought to be formed mainly by open ocean convection in the northern Red Sea [*Sofianos and Johns*, 2003] where salinities close to 40 psu conspire to form a hypersaline outflow at the bottom of the strait. The RSOW layer flows to the south and out of the basin and is characterized by relatively high dissolved oxygen concentration, which close to the Bab el Mandeb area is located at about 150 m depth. It outflows from the basin through the strait of Bab el Mandeb and spreads into the Indian Ocean influencing stratification over an extensive area [*Sofianos and Johns*, 2007]. Its annual mean outflow, estimated at 0.36 Sv, is a good indication of the overall strength of the exchange across the strait of Bab el Mandeb, however, it has a large annual cycle ranging from 0.6 Sv in winter (February) to less than 0.1 Sv in summer (August) [*Sofianos and Johns*, 2007] when there is the summer-time transition to a three-layer exchange, with a shallow surface outflow, the presence of an intermediate fresher and cooler inflow from the Gulf of Aden (GAIW) and a greatly diminished deep outflow of RSOW [*Murray and Johns*, 1997; *Yao et al.*, 2014a,2014b; *Zhan et al.*, 2014]. The central Red Sea basin is dominated by wind-driven forcing and both semi-permanent and transient anticyclonic and cyclonic vortexes with speeds of up to 0.5 m s^{-1} are found, in contrast to the climatological mean along-axis flow of about 0.1 m s^{-1} [*Patzert*, 1974].

3. Methodology

In this section, we describe the Red Sea regional ocean model, the configuration of our model experiments and our approach to implementing dust aerosol effects through shortwave and longwave forcing.

3.1. Model

The Red Sea model is based on the COAWST (Coupled-Ocean-Atmosphere-Wave-Sediment Transport Modeling System) implementation of ROMS (Regional Ocean Modeling System). ROMS is widely used for shelf circulation applications [e.g., *Dinniman et al*., 2003; *Lutjeharms et al*., 2003; *Marchesiello et al*., 2003; *Peliz et al*., 2003; *Warner et al*., 2008, 2010; *Wilkin*, 2006] and more recently to investigate the effects of unsteady mountain-gap winds on eddies in the Red Sea [*Farley Nicholls et al*., 2014]. ROMS employs the split-explicit separation of barotropic and baroclinic modes, and is formulated in vertically stretched terrain-following coordinates. Its computational kernel [*Shchepetkin and McWilliams*, 1998, 2003, 2005] produces accurate, conservative evolution of tracer fields. It includes high-order advection and time stepping schemes, weighted temporal averaging of the barotropic mode to reduce aliasing into the baroclinic motions, and a redefinition of the barotropic pressure-gradient terms to account for local variations in the density field. Vertical discretization uses conservative parabolic splines.

The Red Sea model domain encompasses the entire Red Sea basin and a portion of the Gulf of Aden (Figure 1). The model grid is defined on curvilinear coordinates, rotated along the axis of the Red Sea basin, such that along-basin and across-basin refer to the direction along and across the axis of the basin, respectively. The grid has a 2 km horizontal resolution and 20 terrain-following vertical levels stretched to give increased resolution near the surface. This is sufficient to capture the dominant mesoscale dynamics governing basin-wide circulation. The open boundary is in the east of the Gulf of Aden. This is treated with temperature, salinity, and nontidal velocity fields taken from daily averages of the HYbrid Coordinate Ocean Model (HYCOM) data assimilation product developed as part of the Global Ocean Data Assimilation Experiment "best-estimate" analysis for 2003 to the present [*Chassignet et al*., 2007]. Tides are introduced at the boundary and a Flather boundary condition is imposed for 2-D momentum and radiative nudging for 3-D fields [*Flather*, 1976]. Vertical turbulent mixing closure uses the generic length scale vertical mixing scheme [*Umlauf and Burchard*, 2003] implemented via the *k-kl* option of *Warner et al*. [2005].

For our numerical experiments, we use an ocean-atmosphere boundary layer option, where wind stress, surface net heat, and water fluxes are computed from atmospheric fields using the bulk flux parameterizations of *Fairall et al*. [2003]. We use three hourly output from coincident off-line WRF (Weather Research and Forecasting Model) simulations to calculate atmospheric boundary conditions at the ocean surface. These include downward longwave, downward minus upward shortwave, surface air temperature, surface pressure, specific humidity, precipitation rate, and wind fields at 10 m height. The model computes outgoing longwave radiation as a function of SST, as well as latent and sensible heat fluxes as per *Fairall et al*. [1996]. We recognize that there are limitations in our uncoupled numerical experiment setup and clarify the study as an upper limit sensitivity study on the impact of summertime dust perturbations on the seasonal response of the Red Sea. By prescribing atmospheric variables independently of the dust forcing, we are missing important feedbacks on the net surface energy fluxes which arise from both vertical and horizontal adjustment processes in the atmosphere. We discuss in more detail the consequences of this on our results in section 5. Here we simply explain our sensitivity study as the uncoupled upper ocean response to strong summertime dust perturbation.

The setup which constitutes our control run, hereinafter referred to as CTRL, is as follows: the model is spun up for 7 months and then run for two years for the period corresponding to 1 June 2009 to 31 December 2011. We consider 7 months to be sufficient spin up period given our interest is in short-term seasonality of upper ocean processes in the Red Sea.

3.2. Model Experiments/Dust Aerosol Forcing

For the purposes of our study, we are interested in the impact of the summer-time dust loading on the Red Sea temperature and circulation and the subsequent adjustment of these processes in response to CTRL dust levels throughout the rest of the year. We therefore designed a model experiment, herein referred to as DUST, using the summer-time *Brindley et al*. [2015] estimates (June, July, and August) of shortwave and longwave direct radiative forcing (as a proxy for dust) to perturb the WRF-derived summer-time radiative fluxes used in the CTRL experiment. The *Brindley et al*. [2015] climatology of direct radiative forcing is derived from 5 years of aerosol optical depth (AOD) retrievals from the Meteosat Second Generation SEVIRI (Spinning Enhanced Visible and InfraRed Imager) instrument.

For the DUST experiment, the shortwave and longwave three hourly WRF output fields are scaled as follows to define the perturbed diurnally varying fluxes, F^{SW}_{DUST} and F^{LW}_{DUST}, at the ocean surface:

$$F^{SW}_{DUST}(x,y,t)=F^{SW}_{CTRL}(x,y,t)\left[1+\frac{\Delta F^{SW}(x,y,t)}{F^{SW}_{CTRL}(x,y,t)}\right]$$
$$F^{LW}_{DUST}(x,y,t)=F^{LW}_{CTRL}(x,y,t)\left[1+\frac{\Delta F^{LW}(x,y,t)}{F^{LW}_{CTRL}(x,y,t)}\right] \quad (1)$$

where

1. $F^{SW}_{CTRL}(x,y,t)$ and $F^{LW}_{CTRL}(x,y,t)$ are the total (down-up) shortwave and downward longwave *three* hourly WRF output fields used in the CTRL runs,
2. $\Delta F^{SW}(x,y,t)$ and $\Delta F^{LW}(x,y,t)$ are the daily mean clear sky dust shortwave and longwave radiative forcings at the surface (Figure 2), respectively, and
3. $\overline{F^{SW}_{CTRL}(x,y,t)}$ and $\overline{F^{LW}_{CTRL}(x,y,t)}$ are the daily mean net shortwave and downward longwave WRF fluxes used in the CTRL runs.

The zonal mean summer-time radiative flux forcing computed from the *Brindley et al*. [2015] estimates (Figure 2) highlights the magnitude of the meridional gradient of the radiative flux forcing over the region in summer. In autumn and winter, a much weaker north south gradient in dust levels is evident with the total dust-induced radiative cooling at the surface finally relaxing to between -20 W m^{-2} (north) and -30 W m^{-2} (south) in winter (Figure 2).

In the DUST experiment, dust is turned on abruptly at the beginning of June and switched off at the end of August. The effect of dust outbreaks in other seasons is not considered in either the DUST or CTRL experiment. Clouds are not accounted for in either experiment. The radiative effect of dust was specifically simplified. The DUST experiment was run for the same time period as the CTRL experiment. In both cases, we saved computed daily averages of surface heat fluxes, longwave (LW_DOWN-LW_UP), latent, and sensible, so that we could examine the specific response of these individual fluxes to the dust perturbation further.

4. Results

The following results are based on the two year mean output from 2010 and 2011 CTRL and DUST model runs. First, we present the climatological baseline of the ocean state and an overview of the thermohaline circulation, as capture by our CTRL runs. We specifically examine the model SST, mixed layer depth (MLD), MLD temperature, 75 m temperature, salinity, density, surface currents, buoyancy frequency, surface heat fluxes, and meridional heat transports. We calculate MLD using the temperature criterion, $\Delta T = 0.5$°C, after *Levitus* [1982]. We then present the response of the climatological baseline of the ocean state, the thermohaline circulation and the annual heat budget to the summer-time dust perturbation. We additionally estimate the adjustment of different surface heat fluxes in response to surface cooling, and the adjustment time scale of surface and subsurface temperatures.

4.1. Climatological Baseline of Ocean State

Previous observations and modeled estimates of the Red Sea portray a basin with a clear north to south gradient in sea surface temperature (SST), sea surface salinity (SSS), and surface density throughout the seasons [*Sofianos and Johns*, 2007; *Yao et al*., 2014a,2014b]. The northern part of the basin is typically characterized by higher densities determined by both cooler surface temperatures and higher surface salinity waters. Our CTRL run results are consistent with previous descriptions. The north Red Sea tends to be cooler than the south Red Sea, by about 2°C throughout the seasons (Figure 3). SSTs across the basin as a whole warm up in the summer as the surface heat flux increases. Mean winter SST is 25.7°C in the northern Red Sea and 28°C in the southern Red Sea. In summer, SST has risen to 29.7°C in the northern Red Sea and 31.9°C in the southern Red Sea. Averaged over the whole basin, there is a 4°C rise in SST between winter and summer.

We extract output from the AMSR-OISST data product [*Reynolds et al*., 2007] using the time period June 2009 to December 2011 to evaluate our model results. The CTRL annual mean SST sea basin and subregional estimates are in good agreement with annual mean sea basin and subregional estimates calculated using the AMSR-OISST data product (Figure 3). Comparing model versus data product annual mean SST for the

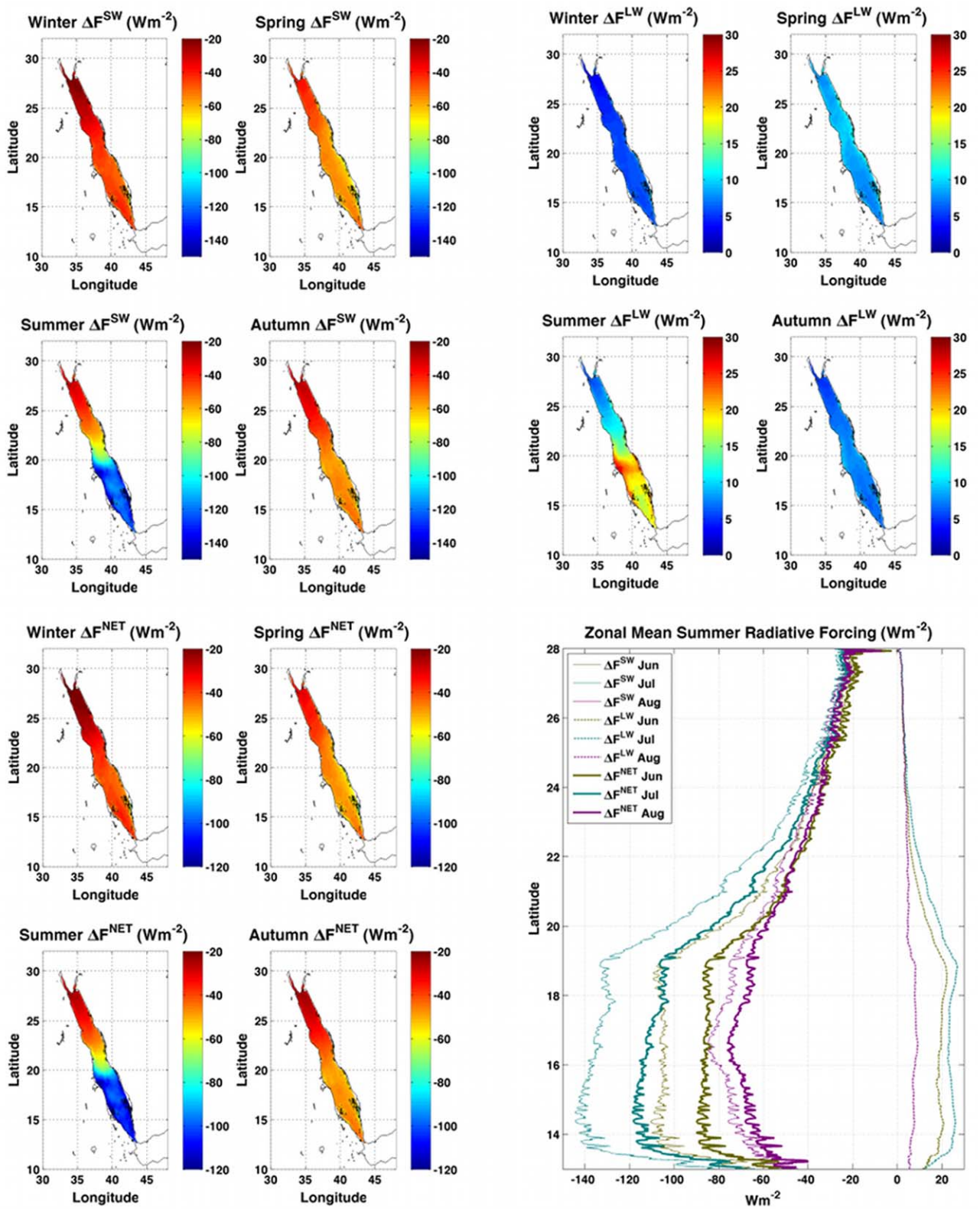

Figure 2. Daily mean seasonal shortwave, longwave, net (shortwave + longwave) radiative forcing at the surface; zonal mean summer radiative forcing, (after *Brindley et al.* [2015] climatology).

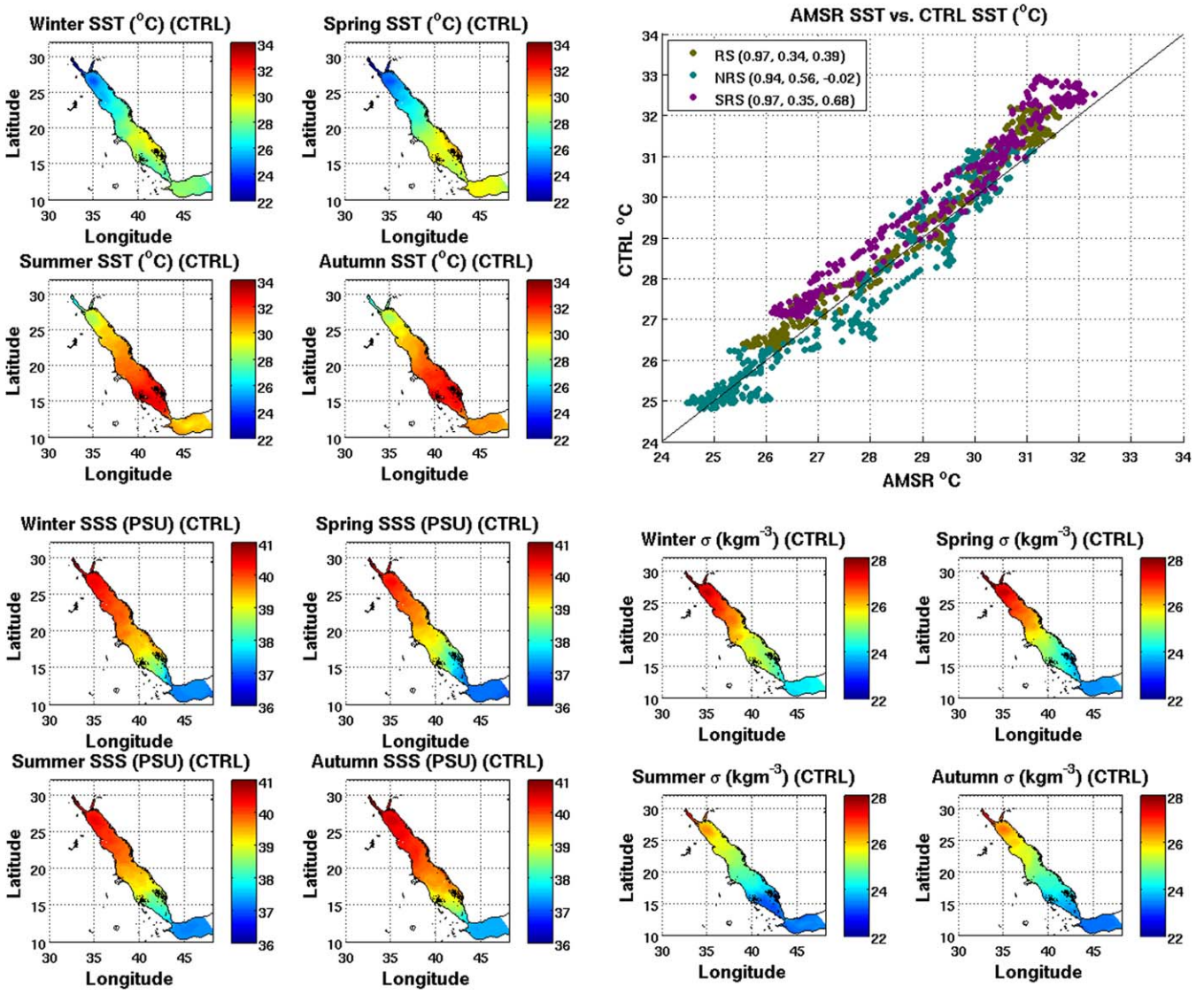

Figure 3. Seasonal mean CTRL SST; CTRL SST versus AMSR-OISST product [*Reynolds et al.*, 2007] (numbers in the legend denote r^2, root-mean-square error and bias statistics, respectively; (N/S)RS denotes (Northern/Southern) Red Sea); CTRL sea surface salinity (SSS); CTRL surface density anomaly.

whole Red Sea, we have an $r^2 = 0.97$, rmse = 0.34, and bias = 0.39. Looking at the model versus data product comparison for the subregions, the annual mean area averaged SSTs in the northern and southern Red Sea have similar r^2, 0.94 and 0.97, respectively, but there are important differences between the subregions in their bias and rmse statistics. The northern Red Sea simulated SSTs ($r^2 = 0.94$, rmse = 0.56, bias = −0.02) are slightly underestimated (small negative bias) and tend to deviate more from the AMSR-OISST product (larger rmse) than the southern Red Sea. The southern Red Sea SSTs ($r^2 = 0.97$, rmse = 0.35, bias = 0.68) tend to be consistently overestimated (larger positive bias).

Our CTRL run surface salinities are indicative of Red Sea Surface Water (RSSW) properties found by *Sofianos and Johns* [2007] and *Yao et al.* [2014a,2014b]. The CTRL estimates range from 36.5 PSU in the southern Red Sea to 40 PSU in the northern Red Sea (Figure 3). Similarly, seasonal surface density plots reflect the along-basin north south gradient and evolving surface warming in the summer months (Figure 3).

Seasonal temperature and salinity sections for the top 300 m along the main axis of the Red Sea basin reveal a thermohaline structure which drives the large-scale flow in the upper and deep layers in the northern Red Sea (Figure 4). An along-basin gradient in temperature and salinity is clear, with warmer, fresher waters persisting in the southern Red Sea. The intrusion of fresher Gulf of Aden waters across the Bab el

Mandeb can be seen in spring and summer. Several interesting features of the thermal-structure are evident, which are consistent with the corresponding seasonal mean surface currents shown in Figure 4. There is a doming of isotherms that persists throughout the seasons at 27°N. This is indicative of upwelling of colder water resulting from a permanent cyclonic feature at this latitude. The average speed of this feature is between 0.3 and 0.5 m s^{-1}, being greatest in winter.

At ca. 19°N, there is a depression of isotherms that is particularly strong in summer and autumn, consistent with downwelling of warmer surface water resulting from a semipermanent anticyclonic vortex at this location. Water temperatures in excess of 30°C are found up to 150 m deep at this location. These features and their origins have been previously observed and documented [*Quadfasel and Baudner*, 1993; *Sofianos and Johns*, 2007; *Zhan et al*., 2014; *Farley Nichols et al*., 2014; *Yao et al*., 2014a,2014b]. Anticyclonic features are predominantly driven by wind-driven circulation in the northern and central parts of the Red Sea basin [*Farley Nichols et al*., 2014; *Sofianos and Johns*, 2007, 2003], while cyclonic features are predominantly driven by thermohaline forcing [*Sofianos and Johns*, 2007, 2003]. The permanent cyclonic feature observed in the North Red Sea is understood to play a critical role in the formation of Red Sea Overflow Water (RSOW) [*Sofianos and Johns*, 2003].

There is evidence of an asymmetric eddy dipole located in the vicinity of the Tokar mountain-gap, ca. 19°N, especially in winter. *Farley Nicholls et al*. [2014] have shown that these arise as a result of Ekman pumping caused by a positive wind stress curl to the left of a mountain-gap wind jet and a negative wind stress curl to the right. This results in a weaker cyclonic feature with a negative sea level anomaly to the left and a stronger anticyclonic feature with a positive sea level anomaly to the right of the mountain-gap wind jet. The asymmetry in the eddy dipole arises from an oscillatory wind field.

Our CTRL runs capture the seasonal cycle of the flow pattern across Bab el Mandeb and are consistent with previous observations and studies. *Murray and Johns* [1997] confirmed that the southern Red Sea exhibits a relatively simple inverse-estuarine, two-layer exchange pattern in winter, which transitions to a more complex three-layer exchange pattern in summer. In the southern Red Sea, coastal intensification of the surface flow into the Red Sea basin through the Bab el Mandeb strait is seen in winter and spring along the west side of the basin (Figure 4). These coastal jets exceed 0.6 m s^{-1} in winter, slowing down to 0.4 m s^{-1} in spring (Figure 4). In summer, this flow pattern reverses and a somewhat slower coastal outflow from the Red Sea through the Bab el Mandeb strait is seen along the east side of the basin, with speeds in the region of 0.2 m s^{-1} (Figure 4). In autumn, a slow coastal inflow along the west side of the basin starts to re-establish itself (Figure 4).

Cross sections of along-basin velocities across the Bab el Mandeb (Figure 5) indicate a two-layer flow pattern in winter and spring. A surface mean inflow of Gulf of Aden Intermediate Water (GAIW), ca. 0.4 m s^{-1} extending up to 20 m in depth in winter overlies a similar mean outflow extending up to 140 m in depth. This flow pattern persists in spring but both the surface inflow and deeper outflow are somewhat weaker, ca. 0.2 m s^{-1}. In summer, the flow pattern changes to a three-layer structure, with a mean surface outflow in the upper 10 m of approximately 0.2 m s^{-1} overlying of a subsurface intrusion of GAIW, ca. 0.2 m s^{-1}, and a much weaker, almost vanishing outflow at depth. In autumn, the two-layer flow pattern observed in spring and winter resumes. This seasonally reversing flow pattern is accompanied by a weakening of the vertical density structure in spring and summer (Figure 5).

4.2. Modeled Seasonal Cycle of the Heat Flux Components

The annually averaged total heat flux into the Red Sea from the atmosphere is characterized by a clear gradient along the axis of the basin; the northern region loses heat while the southern region gains heat (Figure 6). There is considerable seasonality contained in these estimates, determined for the most part by insolation and latent heat flux (Figure 6). The total heat flux is negative in winter in the southern region and in the northern region—also in late autumn and early spring.

Overall, our estimate of the annual total heat flux integrated over the whole Red Sea basin indicates a loss of -17.3 W m^{-2}. This is somewhat comparable to the estimate of *Tragou et al*. [1999] of -8 ± 2 W m^{-2} and is even closer to the estimate of *Sofianos et al*. [2002] of -11.5 ± 5 W m^{-2}. The net energy loss is compensated by the advection of warm water from the Arabian Sea.

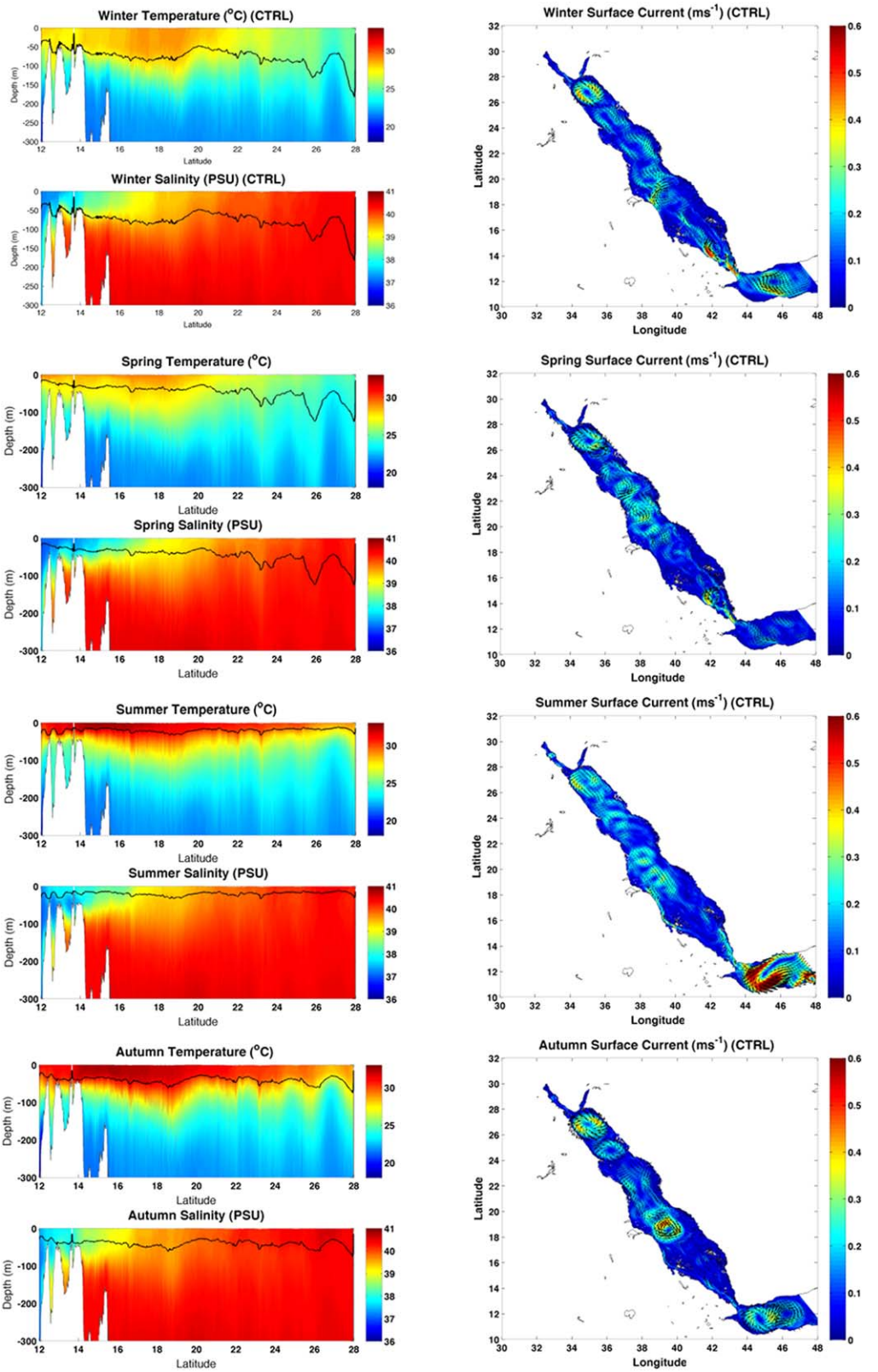

Figure 4. (left) Seasonal meridional temperature and salinity cross sections along axis of Red Sea basin (CTRL), black solid line denotes mixed layer depth (MLD) and (right) corresponding seasonal surface currents (m s^{-1}).

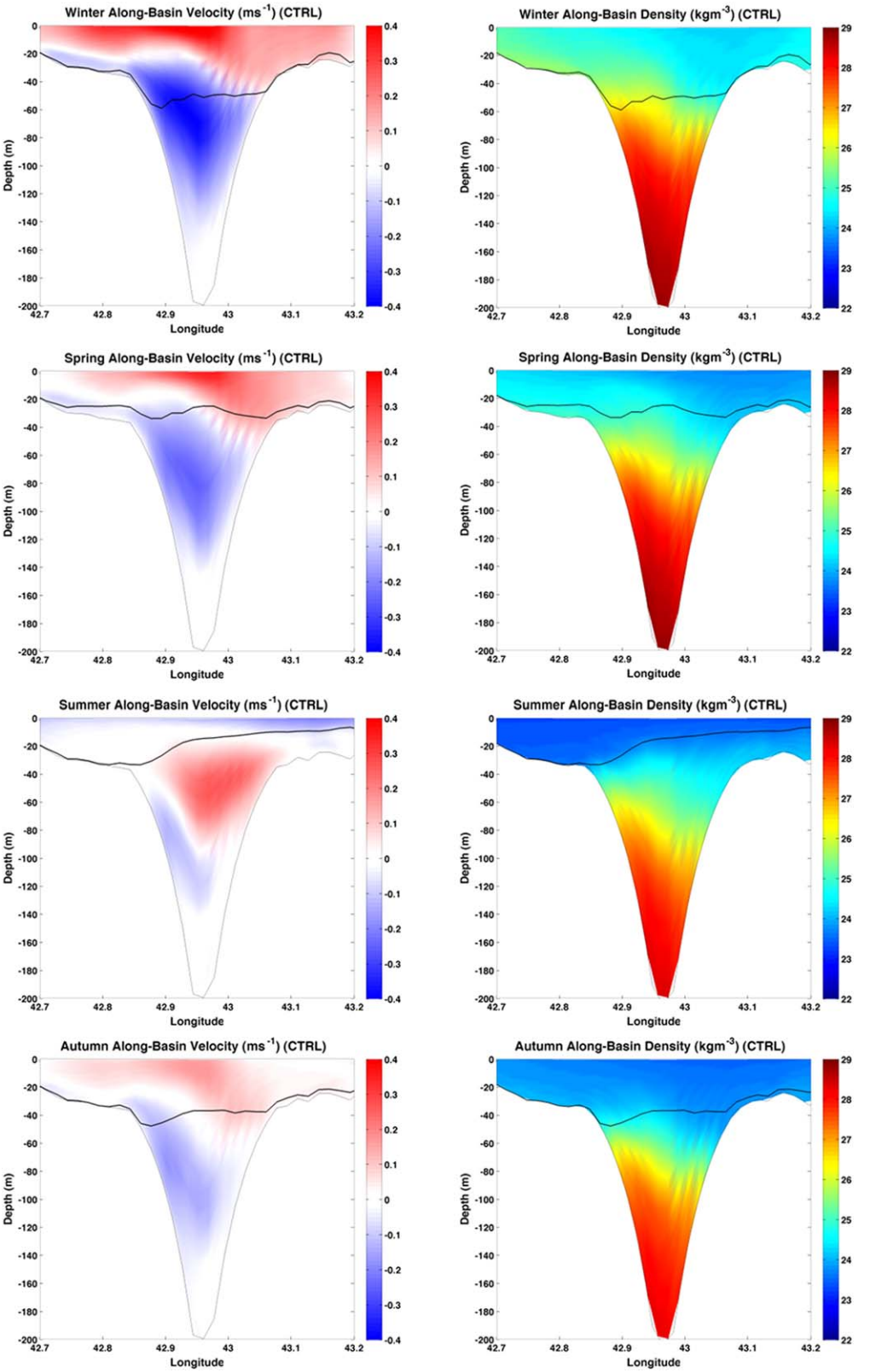

Figure 5. (left) Seasonal along-basin velocity (m s^{-1}) and (right) density (kg m^{-3}) across Bab el Mandeb (CTRL), black solid line denotes mixed layer depth (MLD).

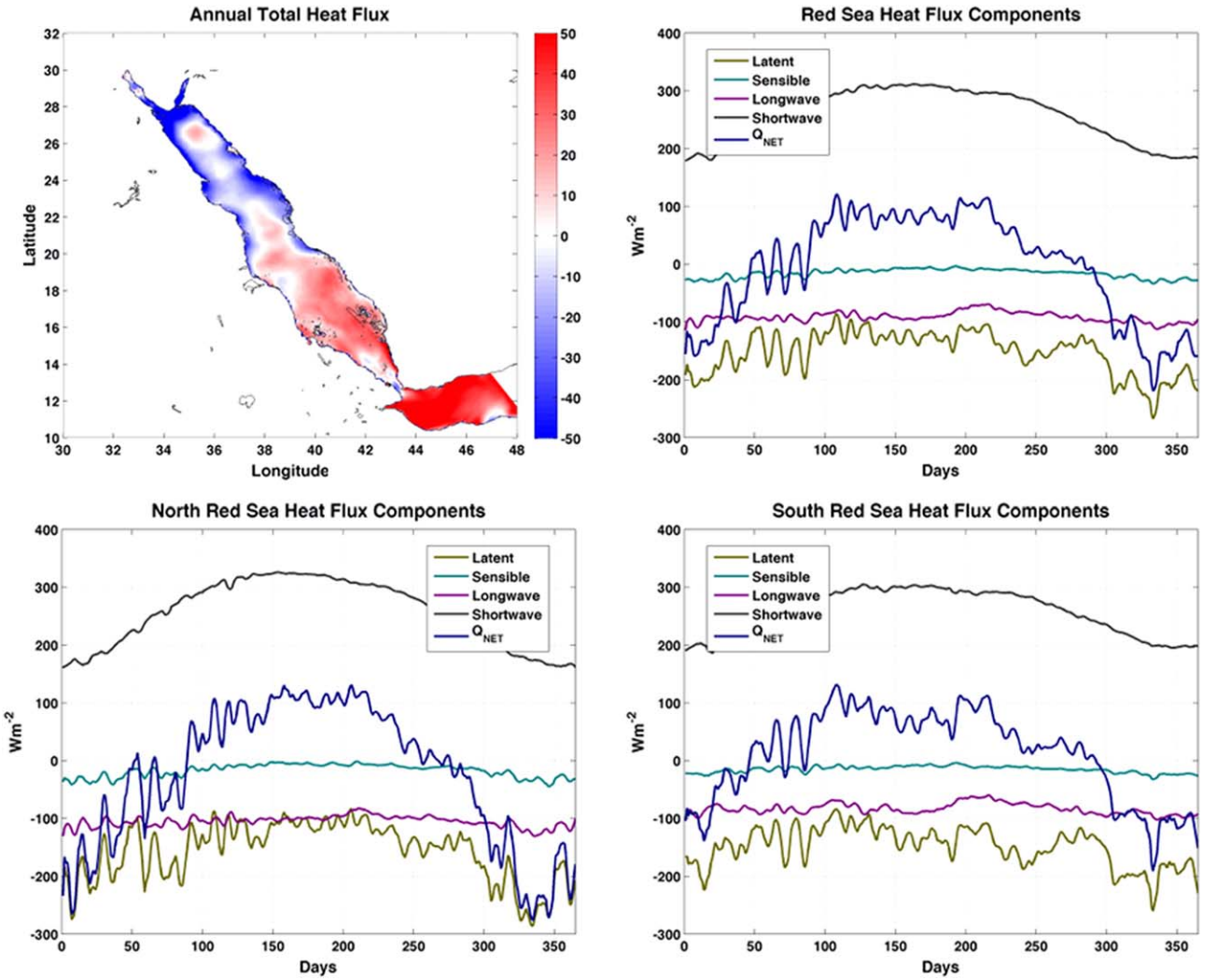

Figure 6. Annual average total heat flux in the CTRL runs; heat flux components over the whole Red Sea; North Red Sea; South Red Sea.

4.3. Impact of Summer-time Dust Aerosols on Ocean State and Heat Budget

4.3.1. Ocean State

The responses of the SST, mixed layer temperature, and 75 m temperature in the northern and southern Red Sea regions to summer-time dust aerosol perturbations are shown in Figure 7 (top). Overall, there is a cooling of the SST. This peaks in the summer, by −1.1°C in the north and −2°C in the south (Table 1). The largest SST cooling is seen at the end of August, −1.6°C in the north and −2.7°C in the south (Figure 7, top). The mixed layer temperature also cools in the summer, by −0.4°C in the north and −1.7°C in the south, while the 75 m temperature cooling in summer is −0.4°C in the north and −0.8°C in the south. The summer mean mixed layer depth is shallower by −0.2 m in the north and by −2.3 m in the south (Figure 7, bottom). By autumn, there is evidence of some adjustment by the surface temperatures to this cooling. The SST cooling anomaly reduces to −1°C both in the north and the south, while, the corresponding 75 m (and mixed layer depth temperature) cooling anomaly is −1.2°C (−0.2°C) in the north and −1.9°C (−1.6°C) in the south, indicating a much slower subsurface adjustment taking place, especially below the mixed layer depth. In fact, while the mixed layer temperatures start to slowly adjust in autumn back to CTRL values, cooling below the mixed layer persists well into late autumn. The corresponding mixed layer depths are even shallower in autumn, by −8 and −7 m in the north and south, respectively. The response of the southern basin is evidently more pronounced than the northern region because the dust-induced radiation perturbation is larger in the southern region (Figure 2) and because the southern region mixed layer depth is shallower and thus more sensitive than the northern one.

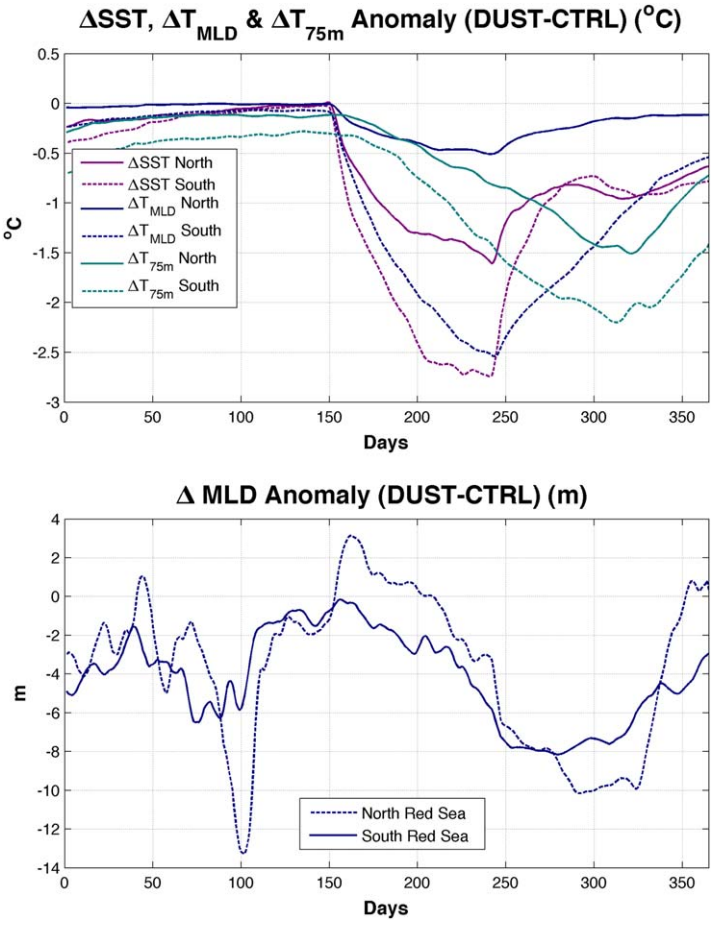

Figure 7. (top) SST anomaly (ΔSST), mixed layer temperature anomaly (ΔT_{MLD}), and 75 m temperature anomaly (ΔT_{75m}), (°C) (DUST-CTRL); (bottom) Mixed Layer Depth (MLD) anomaly, (m) averaged over north and south Red Sea.

The seasonal temperature and salinity difference in the top 300 m and mixed layer depth difference is shown in Figure 8 for a vertical section along the axis of the basin. The corresponding seasonal mean difference in surface currents is shown in Figure 8. The vertical sections clearly show that the depth to which cooling extends in each season is well beyond the mixed layer depth, penetrating to ca. 150 m in the south and almost 300 m in the north. Local cooling below mixed layer can be up to –3°C in the south and up to −1°C in the north in summer. Subsurface cooling below the mixed layer is particularly strong in the autumn reaching −5°C locally in the south and −3°C in the north, respectively. Salinity is also reduced somewhat by between 0.5 and 1PSU presumably due to weaker evaporation as a result of cooler surface temperatures.

The seasonal difference in surface circulation generally indicates a weakening of surface currents in the northern region and a strengthening of surface currents in the southern region. The flow velocity in the permanent cyclonic feature around 27°N is 0.1 and 0.2 m s^{-1} weaker in summer and autumn (Figure 8), respectively. Meanwhile, coastal circulation is especially enhanced in the summer in the south. The outflow of surface waters intensifies (ca. 0.3 m s^{-1}) along the southern coast of Saudi Arabia and Yemen, while an inflow (ca. 0.3 m s^{-1}) is established along the coast of Eritrea. The strength of the anticyclonic feature observed in the central basin increases by ca. 0.2 m s^{-1} in summer and by as much as 0.4 m s^{-1} in autumn.

4.3.2. Exchange Across Bab el Mandeb

The consequences of cooler, fresher water in response to the dust perturbation are seen in the exchange of water masses across the Bab el Mandeb (Figure 9). Cross sections of summertime along-basin DUST velocities and DUST-CTRL density across the Bab el Mandeb indicate a much stronger surface outflow in the DUST run (ca. −0.4 m s^{-1}) (Figure 9) compared to the CTRL run (ca. −0.1 m s^{-1}) (Figure 5), especially

Table 1. Seasonal Response of SST, Mixed Layer Temperature, 75 m Temperature and Mixed Layer Depth to Dust Aerosol Perturbation Averaged Over North and South Red Sea Regions

	North Red Sea	South Red Sea						
	ΔSST (°C)	ΔT_{MLD} (°C)	ΔT_{75m} (°C)	ΔMLD (m)	ΔSST (°C)	ΔT_{MLD} (°C)	ΔT_{75m} (°C)	ΔMLD (m)
Winter	−0.4	−0.1	−0.5	−1.8	−0.5	−0.3	−0.9	−2.7
Spring	−0.1	−0.0	−0.1	−2.0	−0.1	−0.1	−0.3	−1.6
Summer	−1.1	−0.4	−0.4	−0.2	−2.0	−1.7	−0.8	−2.3
Autumn	−1.0	−0.2	−1.2	−8.0	−1.1	−1.6	−1.9	−7.0

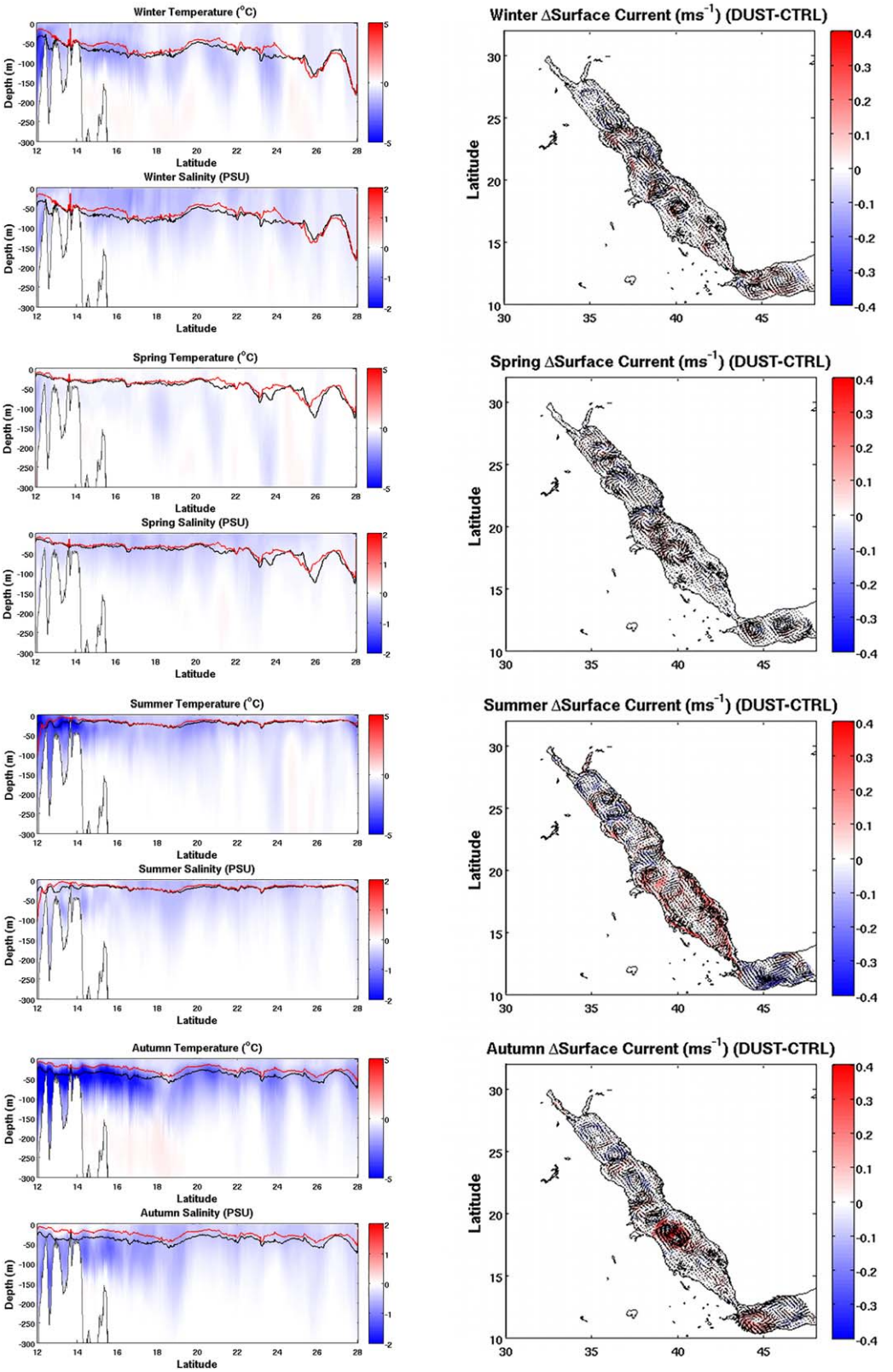

Figure 8. (left) Seasonal meridional temperature and salinity difference cross sections along axis of Red Sea basin (DUST-CTRL) (mixed layer depth, MLD, is shown as solid black (CTRL) and red (DUST) line) and (right) mean difference in surface currents.

in the central and western portion of the basin. The mixed layer depth is much shallower in the DUST run too. In a fully coupled ocean-atmosphere experiment, a shallower mixed layer could be in response to anomalous Ekman pumping arising from wind stress curl perturbations by dust [*Strong et al*., 2015]. However, wind stress curl is not affected by the dust perturbation in our DUST experiment, therefore, the shallower mixed layer is more likely a reflection of increased stratification and mixed layer stability in the upper water column, as noted below (section 4.3.3). In addition, the area over which the subsurface inflow of GAIW penetrates is much larger and shallower in the DUST run which would also account for the reduction in subsurface salinity in the southern Red Sea in the DUST runs (Figure 8). In autumn, the surface inflow of water from the Gulf of Aden almost vanishes along the western portion of the basin in the DUST run but penetrates deeper, to 100 m, along the central and eastern portion of the basin (Figures 5 and 9). Overall, density increases in the DUST runs across the Bab el Mandeb by between 1 and 2 kg m^{-3} in summer and autumn, indicating the stronger impact of cooling on water mass properties (Figure 9).

4.3.3. Stability

The buoyancy frequency (shown for the upper 300 m layer) has been calculated for the top 500 m using 10 m depth bin intervals. Seasonal plots of mean buoyancy frequency (N^2) in the CTRL experiment (Figure 10) and buoyancy frequency difference, DUST-CTRL, (Figure 10) for a cross section along the axis of the basin show clearly the effect of subsurface cooling on the stratification and stability of the water column. The preferentially strong temperature changes subsurface in autumn, lead to a more stable mixed layer and decreased stability below it (Figure 10).

4.3.4. Surface Heat Fluxes

Subsurface cooling exceeds surface cooling in the autumn because the surface can adjust more rapidly by reducing latent and sensible heat losses to the atmosphere, while subsurface adjustment is slower due to increased stratification inhibiting the amount of vertical mixing which can take place. Therefore, the subsurface cooling signal accumulates more effectively and is bigger and lasts longer than at the surface. Figure 11 shows how the individual components of the surface heat fluxes are adjusting in response to the cooling for the northern and southern Red Sea. In the north, the absolute values of the latent and sensible heat fluxes decrease in both the northern and southern Red Sea. In the north, the average summer-time decrease in the absolute value of the latent heat flux is 37 W m^{-2}, while the average summer-time decrease in the absolute value of the sensible heat flux is only 7 W m^{-2}. In the south, a larger adjustment of these heat fluxes is observed. The average absolute value of summer-time latent heat flux decreases by 72 W m^{-2} while the average summer-time sensible heat flux decreases by 14 W m^{-2}. Perturbation of the atmospheric downward longwave flux (LW_DOWN) with the dust signal results in an increase of LW_DOWN. This, coupled with the impact of cooler SST on the outgoing longwave flux (LW_UP), has the net effect of decreasing the summer-time averaged longwave cooling (total LW_DOWN-LW_UP increase) in the DUST experiment by as much as 11 W m^{-2} in the north and 27 W m^{-2} in the south (Figure 11). This effect is closely related to the SST response (see Figure 7, top) and is well seen (especially in South) for the entire autumn season. During the winter, it diminishes due to enhanced vertical mixing.

The adjustment of these fluxes means that energy losses from the ocean due to evaporation are reduced. The largest contributors to ocean temperature relaxation are the latent and longwave fluxes. The sensible heat flux changes sign, while in the CTRL experiment it is on average always from the ocean to the atmosphere, the adjustment of the surface to the DUST perturbations results in positive values of the sensible heat flux in the summer in the southern Red Sea (ca. $+10$ W m^{-2}) indicating that the atmosphere warms the ocean. As a result of all these compensating feedbacks, we find that the response of the average annual total heat flux to the summer-time dust aerosol perturbations is smaller than that of the individual components but it is still significant. It changes from an average annual loss of -17.3 W m^{-2} reported earlier to a small gain of heat reaching $+4.2$ W m^{-2}. This is consistent with the change of sign of the sensible heat flux in summer and the overall reduction in the absolute value of the latent heat and longwave fluxes decreasing the energy loss from the ocean surface.

4.3.5. Heat Transport Along the Axis of the Red Sea Basin

The depth-integrated heat transport is shown in Figure 12 for different transects along the axis of the Red Sea basin (i.e., 13°N, 19°N, 23°N, and 27°N). At 13°N, we see the seasonal northward heat transport in winter, spring, and autumn, with a southward transport in summer. In the DUST experiment, this southward transport increases in late summer, early autumn, consistent with the intensified outward return flow discussed

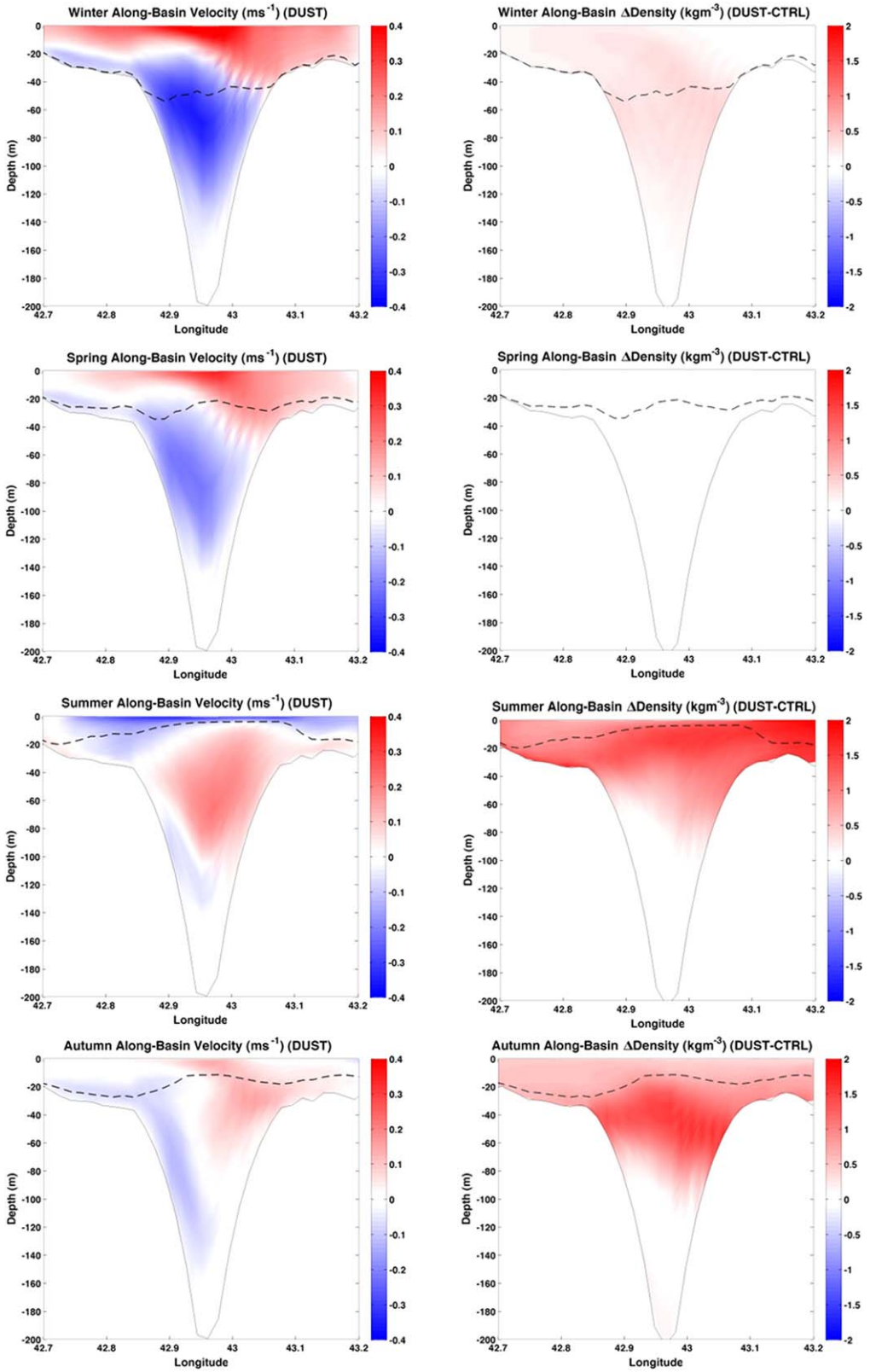

Figure 9. (left) Seasonal along-basin velocity (DUST) and (right) density difference (DUST-CTRL) across Bab et Mandeb, black dashed line denotes DUST mixed layer depth (MLD).

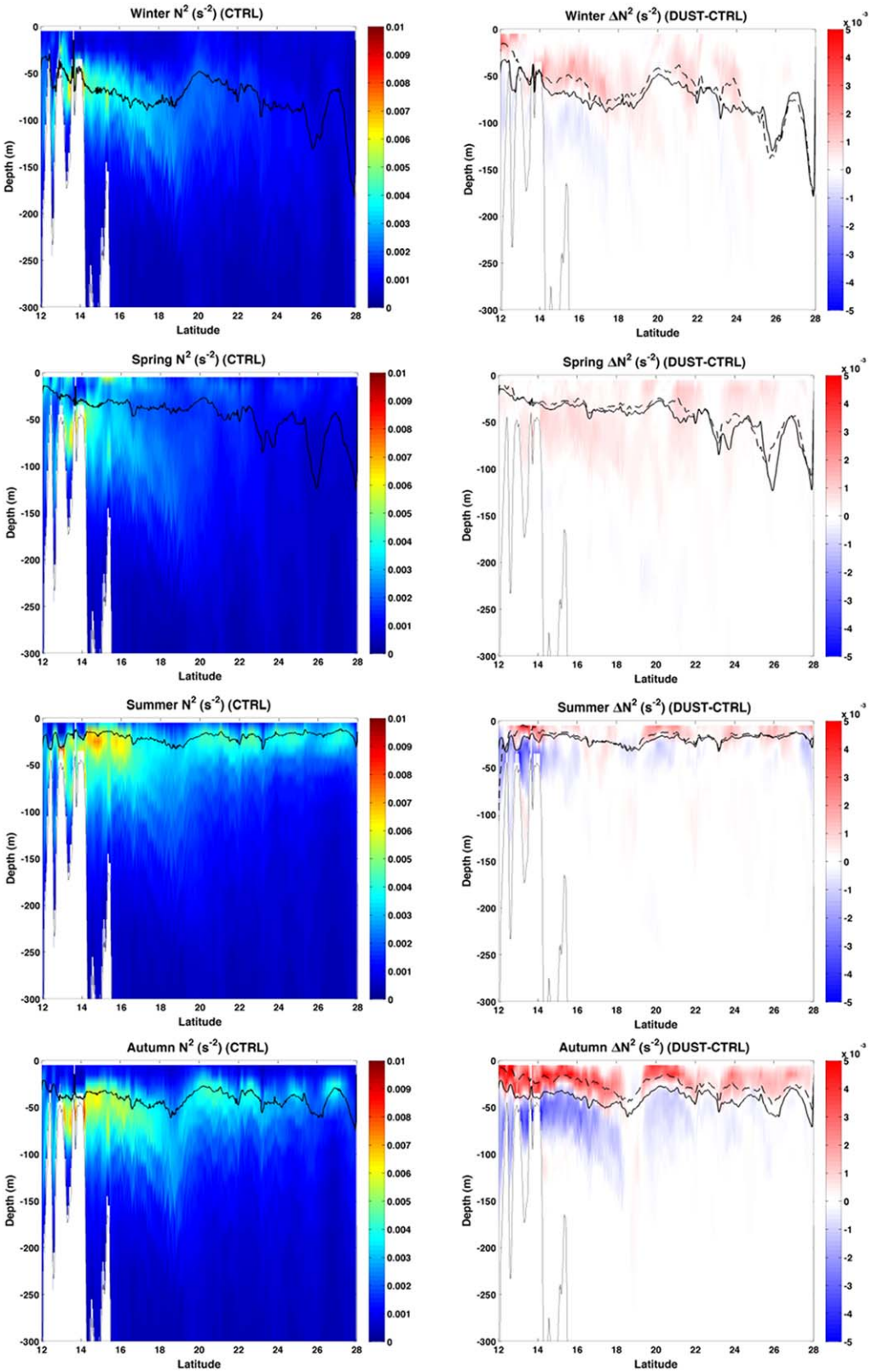

Figure 10. (left) Seasonal buoyancy frequency, N^2 (CTRL) and (right) buoyancy frequency difference (DUST-CTRL) (s^{-2}) across meridional transect along axis of Red Sea basin, (MLD is shown as solid black (CTRL) and dashed (DUST) lines).

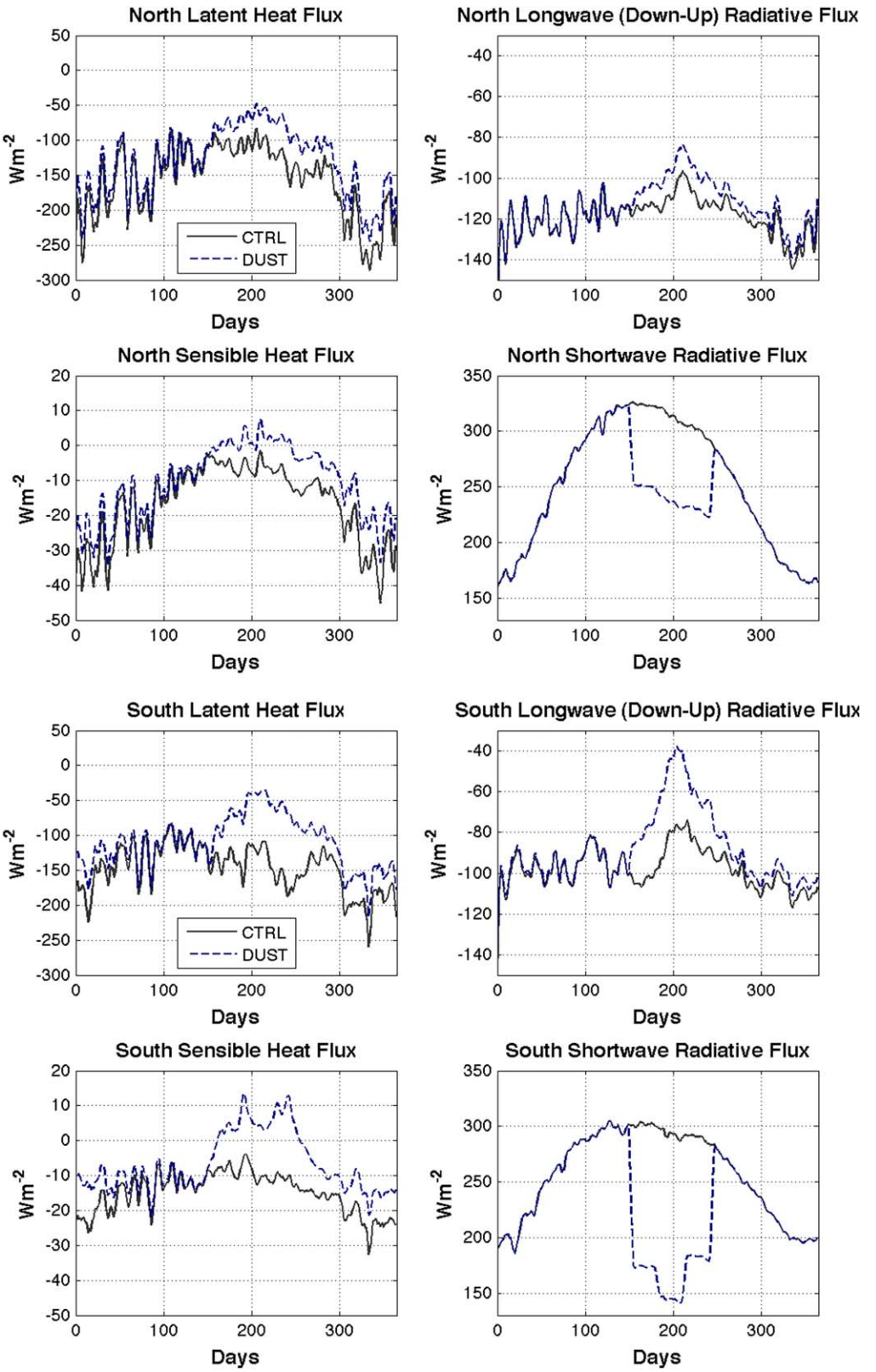

Figure 11. Daily mean radiative flux components (W m^{-2}) for the CTRL (solid gray line) and DUST (dashed blue line) experiments averaged over (top) North Red Sea; (bottom) South Red Sea.

early and the net gain of energy at the surface resulting from the dust perturbation. Integrated annual heat transport is 1.3 TW in the CTRL experiment and less in the DUST experiment, 0.7 TW. At 19°N, heat transport is generally northward with an oscillatory flux pattern that is indicative of the wind-driven eddy features, observed around this location. This pattern shifts in space and changes magnitude in summer in response to the DUST perturbation. At this latitude we see the largest seasonal impact on heat transport from the DUST perturbation, with the peak summer northward heat transport reduced from 30 to 8 GW. However, the annual mean heat transport at this latitude remains almost unchanged, 3.6 TW in the CTRL experiment and 3.4 TW in the DUST experiment. At 23°N, heat transport is weakly northward with an annual mean of 0.9 TW for both the CTRL and DUST experiment. At 27°N, a seasonal northward transport is evident in winter and spring; this reverses in summer and autumn to a southward heat transport. Integrated annual heat transports are southward, −0.1 TW in the CTRL experiment, increasing to −0.4 TW in the DUST experiment.

5. Discussion and Conclusions

In our simulations, we have reproduced the complex seasonal three-dimensional circulation structure in the Red Sea, consistent with previous modeling and observation results [*Yao et al*., 2014a,2014b; *Sofianos and Johns*, 2007]. A permanent cyclonic feature predominantly driven by thermohaline forcing dominates the northern Red Sea, while the circulation in the central and southern Red Sea strongly responds to wind forcing and is dominated by wind-driven anticyclonic features. We perturb the baseline ocean state and further examine the impact of summer-time dust aerosol radiative forcing on the circulation and thermal regime of the Red Sea.

Our results indicate that the Red Sea is highly sensitive to dust-induced reduction in radiative fluxes with important implications for the regional ocean climate, but we qualify this statement by considering the limitations of our uncoupled ocean experiment. The uncoupled DUST experiment is missing several important feedbacks with the atmosphere, which have consequences for the net surface energy flux and ultimately, the degree of surface cooling and time scales for adjustment of the SST anomalies. *Miller* [2012] neatly shows the importance of using a fully coupled model to resolving the magnitude and adjustment time scale of SST anomalies arising from

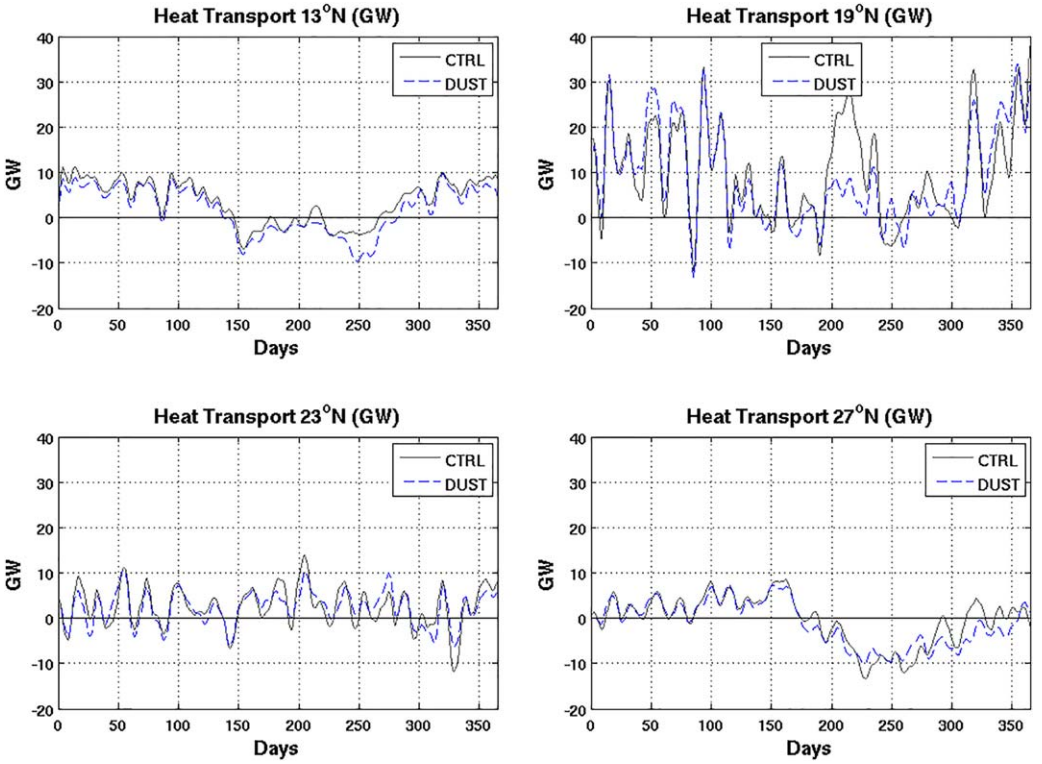

Figure 12. Volume Heat Transport (GW) at 13°N, 19°N, 23°N and 27°N for the CTRL (solid gray line) and DUST (dashed blue line) experiments. Positive values indicate northward transport.

perturbations to radiative forcing. The SST anomaly will depend upon the adjustment of the atmospheric temperature as well as the perturbation to the air-sea temperature difference. In our uncoupled DUST experiment, we only calculate the latter contribution, and then, only under the assumption that the atmospheric state is unchanged by dust. With a fully coupled simulation, the surface air temperature is tightly coupled to the top of atmosphere (TOA) forcing, due to vertical mixing in the atmosphere. This adjustment is transmitted to the ocean via surface forcing and anomalous surface fluxes related to longwave radiation or latent or sensible heating. The atmosphere will adjust quickly compared to the upper ocean, within a week or two and this alters the anomalous flux of total energy into the ocean surface. It is this altered total energy flux (where the rapid adjustment of the atmospheric state to the dust perturbation is taken into account) that the ocean will ultimately respond to. The anomalous surface energy flux will also be different from the original dust surface forcing as a consequence of horizontal atmospheric adjustment to horizontal temperature gradients arising, for example, due to greater dust load over the southern Red Sea, altering the spatial pattern of anomalous surface total energy flux. *Strong et al.* [2015] show how the anomalous surface energy flux over the Atlantic has a different spatial distribution compared to their prescribed North African dust cloud.

We note that the uncoupled DUST SSTs are not in as good agreement as the CTRL SSTs with the AMSR-OISST data product [*Reynolds et al.*, 2007] (Figure 13). The DUST SSTs are also cooler than the AMSR-OISST data product while the CTRL SSTs are generally warmer the AMSR-OISST data product. In actual fact, any observed SST anomaly resulting from dust radiative forcing will be different than that calculated by the uncoupled ocean model. Generally, the effect of atmospheric adjustment upon the ocean increases with the difference between the forcing at TOA and the forcing at the surface [*Miller*, 2012]. This difference equals the atmospheric heating by dust. In the *Brindley et al.* [2015] analysis, atmospheric heating over the Red Sea in the summertime is comparable to the TOA forcing and approximately one half of the surface forcing (see Figure 7) [*Brindley et al.*, 2015], indicating that atmospheric adjustment and its effect upon the ocean response is not negligible. For an equivalent difference between TOA and surface forcing (5 W m^{-2} and 10 W m^{-2}, respectively), *Miller* [2012] shows that the ocean temperature response between a coupled and uncoupled calculation is about half that in the former as the latter (see Figure 13) [*Miller*, 2012]. With this in mind, we infer that a fully coupled ocean-atmosphere DUST experiment would change the magnitude of our SST response significantly. We expect that the magnitude of cooling would be much less, at least half of what we find in the uncoupled experiment. Moreover, the time scale of adjustment would also be shorter as a response to the change in air temperature and surface energy fluxes to the rapid adjustment of the atmosphere. Importantly, the difference in the annual heat budget estimates between the CTRL and the DUST experiments would be much less in a fully coupled DUST experiment. In our uncoupled DUST experiment, the average annual total heat flux reverses sign and becomes positive, indicating a small gain of heat from the atmosphere of +4.2 W m^{-2}, as opposed to a loss of heat to the

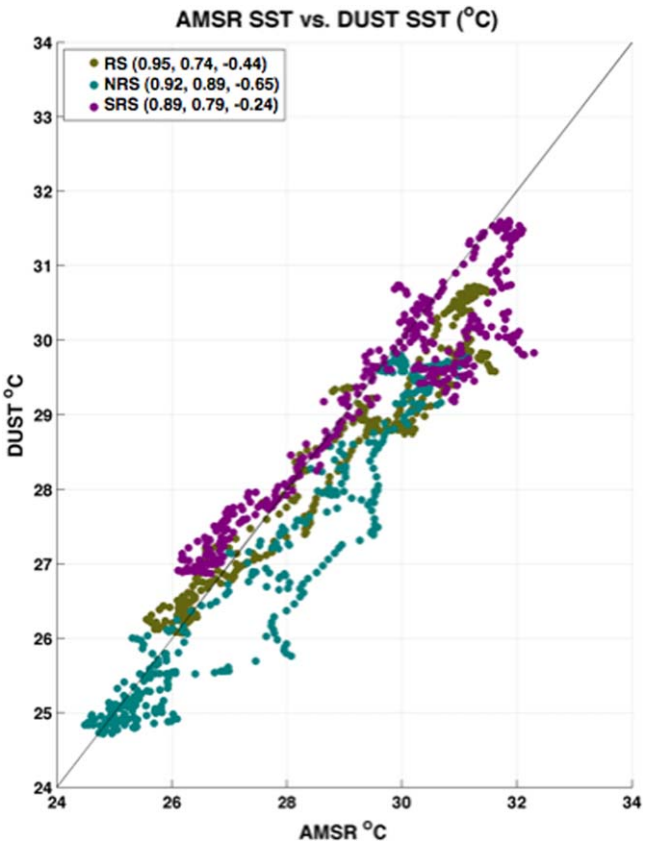

Figure 13. Seasonal mean DUST SST versus AMSR-OISST product [*Reynolds et al.*, 2007] (numbers in the legend denote r^2, root-mean-square error and bias statistics, respectively; (N/S)RS denotes (Northern/Southern) Red Sea.

atmosphere of -17.3 W m^{-2} in the CTRL experiment. We postulate that in a fully coupled experiment, the annual heat budget would not change sign. While it would be smaller in magnitude than that of the CTRL experiment, the Red Sea would remain a source of heat to the atmosphere.

Notwithstanding the limitations outlined above, the results of our uncoupled DUST experiment have some value in that they provide an order of magnitude estimate of the response of the upper ocean to dust-induced radiative forcing perturbations. We find that the ocean surface temperature adjusts more rapidly than the subsurface one, especially in the southern Red Sea, due to a stronger gradient in stratification and increased mixed layer stability inhibiting the extent of vertical mixing. Once the dust perturbation is removed, SST adjusts quickly (within ca. 30 days) while subsurface adjustment requires a longer period and occurs on seasonal time scales. Both surface and mixed layer temperatures return to the original CTRL values by the following spring. This confirms that 2 years of model runs is sufficient to describe the short-term, seasonal effect.

The change in sign of the annual heat budget estimates is due to the longwave, latent and sensible heat fluxes compensating for the cooler SST signal. *Kalenderski et al*. [2013] and *Prakash et al*. [2015] find a reduction in the absolute value of the latent and sensible heat fluxes over land in response to dust-induced radiative cooling (locally ca. -45 W m^{-2} for both fluxes). The larger reduction of sensible heat flux over land compared to the reduction in sensible heat flux over the sea (ca. 7–14 W m^{-2}) is to be expected due to the limited soil moisture available for evaporation in arid regions and the larger fraction of total forcing that the sensible heat flux compensates for [*Miller et al*., 2009].

We also find that an increase in the stratification, reduction of mixed layer depth, which makes the ocean surface more responsive to wind stress, and southward heat transport in the southern Red Sea are accompanied by an intensification of anticyclonic eddies and of the southern coastal currents. Integrated annual heat transports are impacted most at 27°N and 13°N, with an increase in southward heat transport seen at 27°N from -0.1 to -0.4 TW and a reduction in the northward heat transport at 13°N from 1.3 to 0.7 TW in response to the dust perturbation. The reduction in advection of warm water from the Gulf of Aden into the basin in the DUST experiment is related to the shift from annual net energy loss to the atmosphere in the CTRL experiment to annual net energy gain from the atmosphere in the DUST experiment. In the longer term, a persistent net annual heat flux gain resulting from increased dust perturbations could have implications for the direction of the thermohaline circulation and ultimately reverse its direction. We suppose that this would be on the order of at least decadal time scales but cannot go beyond this supposition given the short time frame (2 years) of our experiment.

In this study, we force the Red Sea only with the radiative effect of dust. The surface air temperature remains the same in both the CTRL and DUST experiments. We have noted earlier though that changes in the surface air temperature, and thus, the net energy flux into the ocean, caused by vertical and horizontal adjustment processes in the atmosphere in response to the dust forcing, will further contribute to the overall impact on the Red Sea. However, *Kalenderski et al*. [2013] and *Prakash et al*. [2015] show that air temperature changes in response to dust forcing are moderate and will cause a weaker effect on the Red Sea than the direct radiative effect of dust. We plan to address these processes further in forthcoming regional fully coupled ocean-atmosphere simulations.

The Red Sea has a long history of temperature variations. Since the 1990s, an abrupt warming trend has been observed, $+0.7$°C in the last decade [*Raitsos et al*., 2011]. This phenomenon which is attributed to climate change, is part of a wide spread warming trend observed worldwide [*Alley et al*., 2003]. It is particularly evident in the Red Sea where warming appears to exceed the average marine tropical temperature trends [*Kleypas et al*., 2008]. An increased warming has significantly slowed down the coral growth in the central Red Sea [*Cantin et al*., 2010]. Our study supports the notion that dust aerosols play a profound role in regulating the temperature of the Red Sea at and below the surface. In summer, when dust activity is at its maximum, dust aerosols act as an essential cooling mechanism over the region where otherwise intense insolation could lead to overheating of surface waters and potentially harm the delicate balance of its ecosystem. *Klingmüller et al*. [2016] have studied aerosol optical depth (AOD) trends over the Middle East between 2000 and 2015, and find a positive AOD trend over land in large parts of the Middle East during the period 2001 and 2012 which they relate to increasing temperatures and decreasing relative humidity over land. However, they did not see any positive AOD trend over the Red Sea. Our findings underline the

importance of further understanding the spatial and temporal variability of dust aerosols, their role in regulating the temperature of the Red Sea and the consequences of feedbacks with the marine atmospheric boundary layer for the regional climate.

Acknowledgments
We would like to thank Ron Miller and an anonymous reviewer who provided tremendous insight and exceptionally constructive comments during the preparation of this publication. The research reported in this publication was supported by the King Abdullah University of Science and Technology (KAUST) in Thuwal, Saudi Arabia, by the Natural Environment Research Council and by the BP Environmental Technology Program. The computer resources were partially provided by the KAUST Supercomputing Laboratory. Output of the ROMS simulations used in our analysis is available from Space and Atmospheric Physics, Imperial College London. Contact Bronwyn Cahill (bronwyn.cahill@io-warnemuende.de) or Ralf Toumi (r.toumi@imperial.ac.uk) for further information.

References

Alley, R. B., et al. (2003), Abrupt climate change, *Science*, *299*, 2005–2010, doi:10.1126/science.1081056.
Baars, M. A., P. H. Schalk, and M. J. W. Veldhuis (1998), Seasonal fluctuations in plankton biomass and productivity in the ecosystems of the Somali Current, Gulf of Aden, and Southern Red Sea, in *Large Marine Ecosystems of the Indian Ocean: Assessment, Sustainability, and Management*, edited by K. Sherman, et al., pp. 143–174, Blackwell Science, Oxford, U. K., ISBN: 0632043180.
Belkin, I. M. (2009), Rapid warming of large marine ecosystems, *Prog. Oceanogr.*, *81*, 207–213, doi:10.1016/j.pocean.2009.04.011.
Brindley, H., S. Osipov, R. Bantges, A. Smirnov, J. Banks, R. Levy, P. J. Prakash, and G. Stenchikov (2015), An assessment of the quality of aerosol retrievals over the Red Sea and evaluation of the climatological cloud-free dust direct radiative effect in the region, *J. Geophys. Res. Atmos.*, *120*, 10,862–10,878, doi:10.1002/2015JD023282.
Cantin, N. E., A. L. Cohen, K. B. Karnauskas, A. M. Tarrant, and D. C. McCorkle (2010), Ocean warming slows coral growth in the central Red Sea, *Science*, *329*(5989), 322–325, doi:10.1126/science.1190182.
Chassignet, E. P., H. E. Hurlbert, O. M. Smedstad, G. R. Halliwell, P. J. Hogan, A. J. Wallcraft, R. Baraille, and R. Bleck (2007), The HYCOM (HYbrid Coordinate Ocean Model) data assimilative system, *J. Mar. Syst.*, *65*, 60–83.
Dinniman, M. S., J. M. Klinck, and W. O. Smith Jr. (2003), Cross shelf exchange in a model of the Ross Sea circulation and biogeochemistry, *Deep Sea Res., Part II*, *50*, 3103–3120.
Fairall, C. W., E. F. Bradley, D. P. Rogers, J. B. Edson, and G. S. Young (1996), Bulk parameterization of air-sea fluxes for Tropical Ocean-Global Atmosphere Coupled-Ocean Atmosphere Response Experiment, *J. Geophys. Res.*, *101*(C2), 3747–3764, doi:10.1029/95JC03205.
Fairall, C. W., E. F. Bradley, J. E. Hare, A. A. Grachev, and J. Edson (2003), Bulk parameterization of air-sea fluxes: Updates and verification for the COARE algorithm, *J. Clim.*, *16*, 571–591.
Farley Nicholls, J., R. Toumi, and G. Stenchikov (2014), Effects of unsteady mountain-gap winds on eddies in the Red Sea, *Atmos. Res. Lett.*, *16*, 279–284, doi:10.1002/asl2.554.
Flather, R. A. (1976), A tidal model of the northwest European continental shelf, *Mem. Soc. R. Sci. Liege*, *6*, 141–164.
Grell, G. A., S. E. Peckham, R. Schmitz, S. A. McKeen, G. Frost, W. C. Skamarock, and B. Eder (2005), Fully coupled "online" chemistry within the WRF model, *Atmos. Environ.*, *39*, 6957–6975.
Jiang, H., J. T. Farrar, R. C. Beardsley, R. Chen, and C. Chen (2009), Zonal surface wind jets across the Red Sea due to mountain gap forcing along both sides of the Red Sea, *Geophys. Res. Lett.*, *36*, L19605, doi:10.1029/2009GL040008.
Kalenderski, S., G. Stenchikov, and C. Zhao (2013), Modeling a typical winter-time dust event over the Arabian Peninsula and the Red Sea, *Atmos. Chem. Phys.*, *13*, 1999–2014, doi:10.5194/acp-13-1999-2013.
Kleypas, J. A., G. Danabasoglu, and J. M. Lough (2008), Potential role of the ocean thermostat in determining regional differences in coral reef bleaching events, *Geophys. Res. Lett.*, *35*, L03613, doi:10.1029/2007GL032257.
Klingmüller, K., A. Pozzer, S. Metzger, G. L. Stenchikov, and J. Lelieveld (2016), Aerosol optical depth trend over the Middle East, *Atmos. Chem. Phys.*, *16*, 5063–5073, doi:10.5194/acp-16-5063-2016.
Lau, K. M., and K. M. Kim (2007), Cooling of the Atlantic by Saharan dust, *Geophys. Res. Lett.*, *34*, L23811, doi:10.1029/2007GL031538.
Levitus, S. (1982), Climatological Atlas of the World Ocean, *NOAA Prof. Pap. 13*, U.S. Dep. of Comm., National Oceanic and Atmospheric Administration.
Li, F., and V. Ramanathan (2002), Winter to summer monsoon variation of aerosol optical depth over the tropical Indian Ocean, *J. Geophys. Res.*, *107*(D16), 4284, doi:10.1029/2001JD000949.
Lutjeharms, J. R. E., P. Penven, and C. Roy (2003), Modelling the shear edge eddies of the southern Agulhas Current, *Cont. Shelf Res.*, *23*, 1099–1115.
Marchesiello, P., J. C. McWilliams, and A. F. Shchepetkin (2003), Equilibrium structure and dynamics of the California Current System, *J. Phys. Oceanogr.*, *33*(4), 753–783.
Miller, R. L. (2012), Adjustment to radiative forcing in a simple coupled ocean-atmosphere model, *J. Clim.*, *25*, 7802–7821, doi:10.1175/JCLI-D-11-00119.1.
Miller, R. L., A. Slingo, J. C. Barnard, and E. Kassianov (2009), Seasonal contrast in the surface energy balance of the Sahel, *J. Geophys. Res.*, *114*, D00E05, doi:10.1029/2008JD010521.
Murray, S. P., and W. Johns (1997), Direct observations of seasonal exchange through the Bab et Mandab Strait, *Geophys. Res. Lett.*, *24*(21), 2557–2560.
Osipov, S., G. Stenchikov, H. Brindley, and J. Banks (2015), Diurnal cycle of the dust instantaneous direct radiative forcing over the Arabian Peninsula, *Atmos. Chem. Phys.*, *15*, 9537–9553, doi:10.5194/acp-15-9537-2015.
Patzert, W. C. (1974), Wind induced reversal in the Red Sea circulation, *Deep Sea Res.*, *21*, 109–121.
Peliz, Á., J. Dubert, D. B. Haidvogel, and B. Le Cann (2003), Generation and unstable evolution of a density-driven eastern poleward current: The Iberian Poleward Current, *J. Geophys. Res.*, *108*(C8), 3268, doi:10.1029/2002JC001443.
Phillips, O. M. (1966) On turbulent convection currents and the circulation of the Red Sea, *Deep Sea Res. Oceanogr. Abstr.*, *13*, 1149–1160.
Prakash, P. J., G. Stenchikov, S. Kalenderski, S. Osipov, and H. Bangalath (2015), The impact of dust storms on the Arabian Peninsula and the Red Sea, *Atmos. Chem. Phys.*, *15*, 199–222, doi:10.5194/acp-15-199-2015.
Prospero, J. M., P. Ginoux, O. Torres, S. E. Nicholson, and T. E. Gill (2002), Environmental characterization of global sources of atmospheric soil dust identified with the Nimbus 7 Total Ozone Mapping Spectrometer (TOMS) absorbing aerosol product, *Rev. Geophys.*, *40*(1), 1002, doi:10.1029/2000RG000095.
Quadfasel, D., and H. Baudner (1993), Gyre-scale circulation cells in the Red Sea, *Oceanol. Acta*, *16*(3), 221–229.
Raitsos, D. E., I. Hoteit, P. K. Prihartato, T. Chronis, and G. Triantafyllou (2011), Abrupt warming of the Red Sea, *Geophys. Res. Lett.*, *38*, L14601, doi:10.1029/2011GL047984.
Raitsos, D. E., Y. Pradhan, R. J. W. Brewin, G. Stenchikov, and I. Hoteit (2013), Remote sensing the phytoplankton seasonal succession of the Red Sea, *PLoS One*, *8*(6), e64909, doi:10.1371/journal.pone.0064909.
Reynolds, R. W., T. M. Smith, C. Liu, D. B. Chelton, K. S. Casey, and M. G. Schlax (2007), Daily high-resolution-blended analyses for sea surface temperature, *J. Clim.*, *20*, 5473–5496, doi:10.1175/2007JCLI1824.1

Shchepetkin, A., and J. C. McWilliams (1998), Quasi-monotone advection schemes based on explicit locally adaptive dissipation, *Mon. Weather Rev.*, *126*, 1541–1580.

Shchepetkin, A., and J. C. McWilliams (2003), A method for computing horizontal pressure gradient force in an oceanic model with a non-aligned vertical coordinate, *J. Geophys. Res.*, *108*(C3), 3090, doi:10.1029/2001JC001047.

Shchepetkin, A. F., and J. C. McWilliams (2005), The regional oceanic modeling system (ROMS): A split-explicit, free-surface, topography-following-coordinate oceanic model, *Ocean Modell.*, *9*(4), 347−404.

Skamarock, W. C., J. B. Klemp, J. Dudhia, D. O. Gill, D. M. Barker, W. Wang, and J. G. Powers (2007), A description of the advanced research WRF version 2, *NCAR Tech. Note NCAR/TN-468+STR*, Natl. Cent. for Atmos. Res., Boulder, Colo. [Available at http://www2.mmm.ucar.edu/wrf/users/docs/arw_v2_070111.pdf, last access: November 2015.]

Sofianos, S. S., and W. E. Johns (2003), An oceanic general circulation model (GCM) investigation of the Red Sea circulation. 2: Three-dimensional circulation in the Red Sea, *J. Geophys. Res.*, *108*(C3), 3066, doi:10.1029/2001JC001185.

Sofianos, S. S., and W. E. Johns (2007), Observations of the summer Red Sea circulation, *J. Geophys. Res.*, *112*, C06025, doi:10.1029/2006JC003886.

Sofianos, S. S., W. E. Johns, and S. P. Murray (2002), Heat and freshwater budgets in the Red Sea from direct observations at Bab el Mandeb, *Deep Sea Res., Part II*, *49*, 1323–1340.

Strong, J. D. O., G. A. Vecchi, and P. Ginoux (2015), The response of the tropical Atlantic and West African climate to Saharan Dust in a fully couple GCM, *J. Clim.*, *28*, 7071–7092, doi:10.1175/JCLI-D-14-00797.1.

Tragou, E., C. Garrett, and R. Outerbridge (1999), The heat and freshwater budgets of the Red Sea, *J. Phys. Oceanogr.*, *29*, 2504–2522.

Umlauf, L., and H. Burchard (2003), A generic length-scale equation for geophysical turbulence models, *J. Mar. Res.*, *61*(2), 235–265.

Warner, J. C., C. R. Sherwood, H. G. Arango, R. P. Signell, and B. Butman (2005), Performance of four turbulence closure models implemented using a generic length scale method, *Ocean Modell.*, *8*, 81–113.

Warner, J. C., C. R. Sherwood, R. P. Signell, C. Harris, and H. G. Arango (2008), Development of a three-dimensional, regional, coupled wave, current, and sediment-transport model, *Comput. Geosci.*, *34*, 1284–1306.

Warner, J. C., B. Armstrong, R. He, and J. B. Zambon (2010), Development of a Coupled Ocean-Atmosphere-Wave-Sediment Transport (COAWST) modeling system, *Ocean Modell.*, *35*(3), 230–244.

Wilkin, J. L. (2006), The summer-time heat budget and circulation of southeast New England shelf waters, *J. Phys. Oceanogr.*, *36*(11), 1997–2011.

Yao, F., I. Hoteit, L. J. Pratt, A. S. Bower, P. Zhai, A. Kohl, and G. Gopalakrishnan (2014a), Seasonal overturning circulation in the Red Sea. 1: Model validation and summer circulation, *J. Geophys. Res. Oceans*, *119*, 2238–2262, doi:10.1002/2013JC009004.

Yao, F., I. Hoteit, L. J. Pratt, L. J. Pratt, A. S. Bower, P. Zhai, A. Kohl, G. Gopalakrishnan, and D. Rivas (2014b), Seasonal overturning circulation in the Red Sea. 2: Winter circulation, *J. Geophys. Res. Oceans*, *119*, 2263–2289, doi:10.1002/2013JC009331.

Zhan, P., A. C. Subramanian, F. Yao, and I. Hoteit (2014), Eddies in the Red Sea: A statistical and dynamical study, *J. Geophys. Res. Oceans*, *119*, 3909–3925, doi:10.1002/2013JC009563.